

Article

# Electron Backscatter Diffraction Studies on the Formation of Superlattice Metal Hydride Alloys

Shuli Yan <sup>1,2</sup>, Kwo-Hsiung Young <sup>1,2,\*</sup> , Xin Zhao <sup>3</sup>, Zhi Mei <sup>4</sup> and K. Y. Simon Ng <sup>1</sup>

<sup>1</sup> Department of Chemical Engineering and Materials Science, Wayne State University, Detroit, MI 48202, USA; shuli.yan@partners.basf.com (S.Y.); sng@wayne.edu (K.Y.S.N.)

<sup>2</sup> BASF/Battery Materials—Ovonac, 2983 Waterview Drive, Rochester Hills, MI 48309, USA

<sup>3</sup> School of Materials and Metallurgy, Inner Mongolia University of Science and Technology, Baotou 014010, Inner Mongolia, China; fatcatzx@163.com

<sup>4</sup> Department of Chemistry, Wayne State University, Detroit, MI 48202, USA; zmei@chem.wayne.edu

\* Correspondence: kwo.young@basf.com; Tel.: +1-248-293-7000

Received: 2 October 2017; Accepted: 5 December 2017; Published: 13 December 2017

**Abstract:** Microstructures of a series of La-Mg-Ni-based superlattice metal hydride alloys produced by a novel method of interaction of a LaNi<sub>5</sub> alloy and Mg vapor were studied using a combination of X-ray energy dispersive spectroscopy and electron backscatter diffraction. The conversion rate of LaNi<sub>5</sub> increased from 86.8% into 98.2%, and the A<sub>2</sub>B<sub>7</sub> phase abundance increased from 42.5 to 45.8 wt % and reduced to 39.2 wt % with the increase in process time from four to 32 h. During the first stage of reaction, Mg formed discrete grains with the same orientation, which was closely related to the orientation of the host LaNi<sub>5</sub> alloy. Mg then diffused through the *ab*-phase of LaNi<sub>5</sub> and formed the AB<sub>2</sub>, AB<sub>3</sub>, and A<sub>2</sub>B<sub>7</sub> phases. Diffusion of Mg stalled at the grain boundary of the host LaNi<sub>5</sub> alloy. Good alignments in the *c*-axis between the newly formed superlattice phases and LaNi<sub>5</sub> were observed. The density of high-angle grain boundary decreased with the increase in process time and was an indication of lattice cracking.

**Keywords:** metal hydride; superlattice alloy; electron backscatter diffraction; crystallographic orientation; gaseous-state diffusion; superlattice alloy

## 1. Introduction

Rare earth (RE)/Mg-based superlattice metal hydride (MH) alloys are employed extensively in the consumer nickel/metal hydride (Ni/MH) batteries because of the following improvements over the conventional AB<sub>5</sub> MH alloys: higher hydrogen storage capacities, better high-rate dischargeability (HRD), superior low-temperature and charge-retention performances, and improved cycle stability [1–8]. Out of the six available superlattice phases (three hexagonal and three rhombohedral), Ce<sub>2</sub>Ni<sub>7</sub> was found to be the most desirable phase considering general battery performance [9], and the A<sub>2</sub>B<sub>7</sub> stoichiometry shows the best HRD, charge retention, and cycle life [10]. Although the superlattice MH alloys are very attractive to battery engineers, their fabrication is difficult because of the high vapor pressure of Mg [11]—an indispensable ingredient to maximize the capacity and stabilize the structure [12,13]. In the conventional melt-and-cast method, Mg was added as a late addition in the form of MgNi<sub>2</sub> [14]. Extra Mg needs to be added to compensate for the loss to vapor, which is a difficult factor to control precisely. A new method of making the Mg-containing superlattice MH alloys [15] was proposed using a gaseous-state Mg-diffusion into the AB<sub>5</sub> MH alloys, which can be easily produced by vacuum induction melting with a furnace size as large as one ton [16]. Early electron microscope studies indicated the feasibility of transporting Mg into the La<sub>0.8</sub>Ni<sub>3</sub> alloy and forming the Mg-containing superlattice phases, but the constituent phases have not yet been confirmed [15].

Electron backscatter diffraction (EBSD) is a microstructural-crystallographic technique that allows the user to examine the crystallographic orientations of constituent phases in very localized areas (one square micron or less) of a polycrystalline material in a scanning electron microscope (SEM). Capability of EBSD can be further enhanced by including the chemical composition information gathered by X-ray energy dispersive spectroscopy (EDS) [17]. In the past, we employed EBSD in the studies of a  $Zr_7Ni_{10}$  [18], a C14-based  $AB_2$  [19], and a C14/body-centered-cubic MH alloys [20]. In the last two cases, EBSD was used to confirm the cleanliness of the grain boundary from the strong alignment of crystallographic orientations of neighboring phases. In the current study, EBSD was used to identify the new phases formed by the Mg-diffusion into the  $LaNi_5$  alloy and study the nature of grain boundary and alignment of crystallographic orientations of neighboring phases.

## 2. Experimental Setup

The  $LaNi_5$  alloy was synthesized by induction melting La and Ni (both with purity higher than 99.5%) under an argon atmosphere. Solidification of the  $LaNi_5$  alloy was operated by a rapid quenching equipment to ensure the slice thickness to be between 0.2 to 0.4 mm. The Mg-absorption alloying process was operated in a sealed internal isolation stainless-steel retort. Slices of Mg and  $LaNi_5$  were placed into each side of the retort in a weight ratio of  $Mg:LaNi_5 = 1:30$  and separated by foraminiferous septa. The retort was placed in an annealing furnace under an inert atmosphere (argon). Annealing (reaction) temperature was increased from the ambient temperature to 1273 K with a heating rate of  $10\text{ K}\cdot\text{min}^{-1}$ . Afterward, the vessel was cooled to room temperature in the furnace.

4-h, 8-h, 16-h, and 32-h annealed alloy samples were mounted in resin holders. The samples were polished using metallographic silicon carbide sandpapers in the sequence of 400-, 800- and, finally, 1200-grit (Buehler, Lake Bluff, IL, USA), and they were then finely polished with Buehler MicroPolish II Suspension 1- $\mu\text{m}$  alumina suspension and PACE Technologies SIAMAT2 0.02- $\mu\text{m}$  colloidal silica (PACE Technologies, Tucson, AZ, USA) to obtain a mirror finish. The prepared samples were kept in a sealed tank with high vacuum and low  $O_2^-$  and moisture content to avoid surface oxidization and physical and chemical absorptions.

To investigate the phase distribution, samples were studied by a JEOL JSM-7600 field emission SEM (JEOL USA, Inc., Peabody, MA, USA) equipped with an EDAX Pegasus Apex 2 Integrated EDS and EBSD System (EDAX Inc., Mahwah, NJ, USA). The EBSD data was collected and analyzed with TSL OIM data Collection 7 and TSL OIM Analysis 7 program (EDAX Inc., Mahwah, NJ, USA), respectively. - All the measured points have confidence indices greater than 0.6, which corresponds to an accuracy higher than 95%. Fit parameter is the averaged angular difference between the detected and recalculated bands. In this case, the fit parameter is less than 0.8, showing a high degree of matching.

## 3. Results and Discussion

### 3.1. Phase Identification

As stated in the Introduction, the La-Mg-Ni-type alloys were based on the La-Ni binary intermetallic alloys. The presence of Mg destabilizes the hydride, making it suitable for room-temperature battery applications [13]. Phases commonly reported in the La-Mg-Ni superlattice alloys are  $(La,Mg)Ni_5$ ,  $(La,Mg)_5Ni_{19}$ ,  $(La,Mg)_2Ni_7$ ,  $(La,Mg)Ni_3$ , and  $(La,Mg)Ni_2$ . [21]. Basic subunits for these phases are the  $AB_5$  and  $A_2B_4$  slabs, which alternatively stack along the  $c$ -axis in different patterns to form the structures [21,22]. Six types of the La-Mg-Ni superlattice phases are  $Pr_5Co_{19}$  (PDF: 04-004-1477),  $Nd_5Co_{19}$  (PDF: 04-004-1478),  $Ce_2Ni_7$  (PDF: 04-007-1092),  $Pr_2Ni_7$  (PDF: 01-081-8491),  $CeNi_3$  (PDF: 04-007-1090), and  $PuNi_3$  (PDF: 04-007-1091), and their structures are either hexagonal or rhombohedral and are generally difficult to distinguish in the X-ray diffraction patterns [21–25]. Furthermore, the  $AB_5$  (PDF: 00-055-0277) and  $AB_2$  (PDF: 04-001-2137) phases are also hexagonal, which adds to the difficulty in identifying the phases. EBSD provides a powerful approach to study the lattice structures of individual phases and their alignments in certain orientations in the multi-phase

La-Mg-Ni superlattice alloys. Figure 1 shows the crystal structures and computer-generated EBSD diffraction patterns of the (1120) planes of  $\text{LaNi}_5$ ,  $\text{Pr}_5\text{Co}_{19}$ ,  $\text{Nd}_5\text{Co}_{19}$ ,  $\text{Ce}_2\text{Ni}_7$ ,  $\text{Pr}_7\text{Ni}_2$ ,  $\text{CeNi}_3$ ,  $\text{PrNi}_3$ , and  $\text{NbCr}_2$  (hexagonal), which are used as the base patterns in this study. Lattice parameters of the seven types of structures are different and, therefore, their EBSD patterns are different, especially away from the (0001) plane.

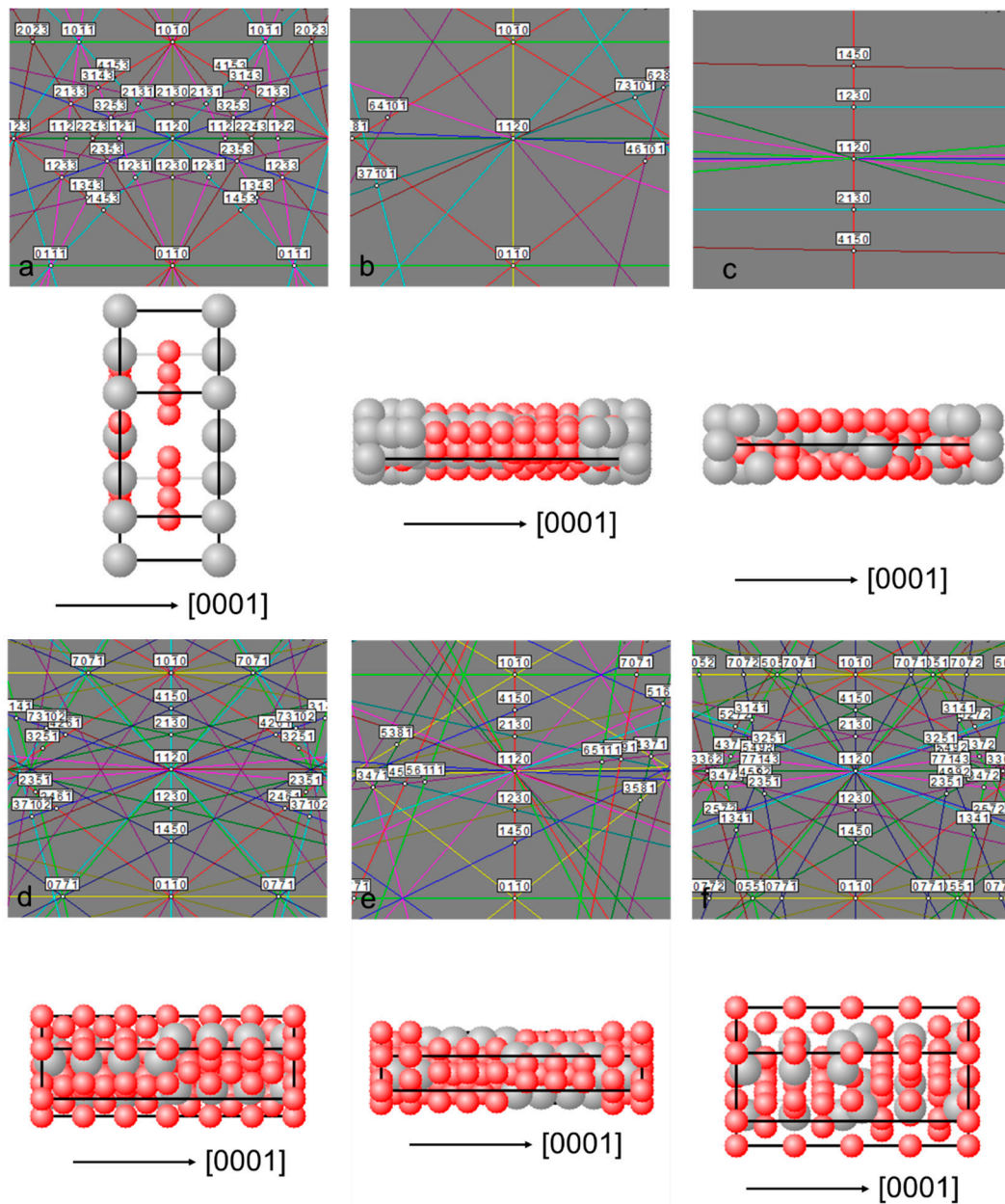
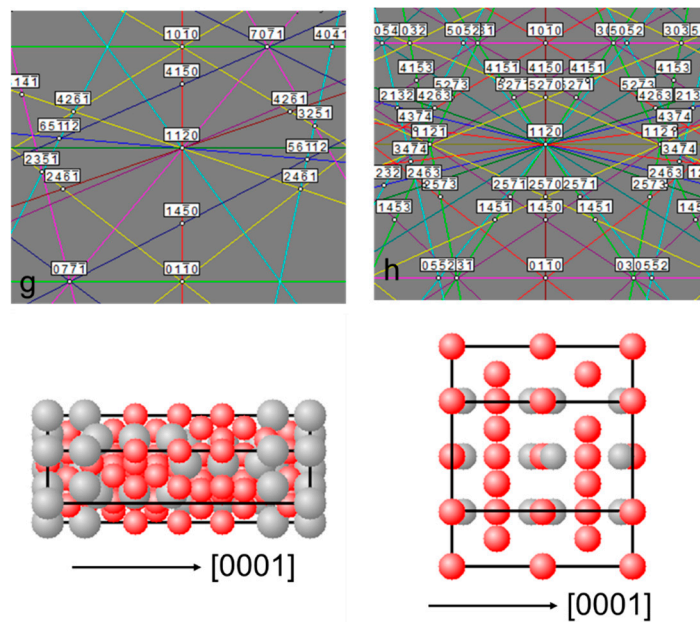
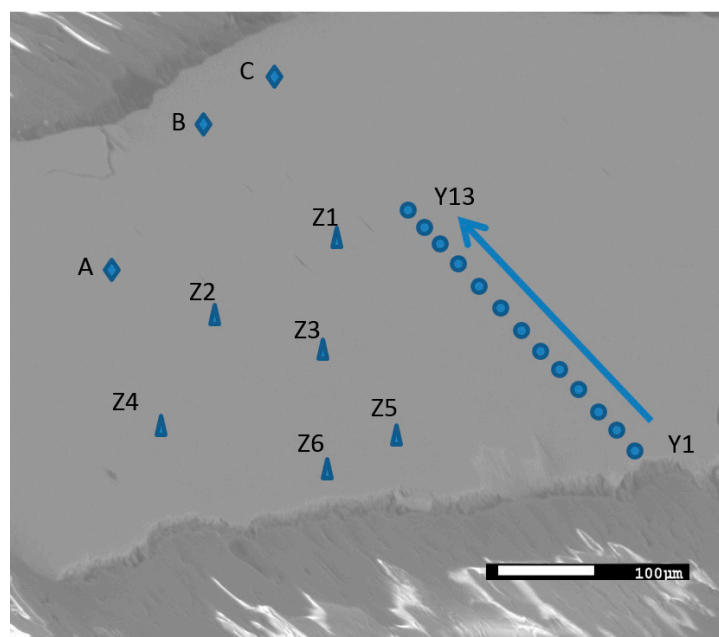


Figure 1. Cont.



**Figure 1.** Computer-generated EBSD patterns for the  $(11\bar{2}0)$  planes of (a)  $\text{LaNi}_5$ ; (b)  $\text{Pr}_5\text{Co}_{19}$ ; (c)  $\text{Nd}_5\text{Co}_{19}$ ; (d)  $\text{Ce}_2\text{Ni}_7$ ; (e)  $\text{Pr}_2\text{Ni}_7$ ; (f)  $\text{CeNi}_3$ ; (g)  $\text{PrNi}_3$ ; and (h)  $\text{NbCr}_2$  (hexagonal).

SEM-backscattered electron image (BEI) of the 8-h annealed sample is shown in Figure 2, and several spots were studied in detail (spots Z1 to Z6, A to C, and Y1 to Y13). For spots Z1 to Z6, their original EBSD patterns, fitted patterns, and simulations of grain orientation are shown in Figure 3. Other than the base structure ( $\text{LaNi}_5$ , spot Z1), both the  $\text{A}_2\text{B}_7$  (spots Z2 and Z3) and  $\text{AB}_3$  (spot Z4) superlattice structures, Mg metal (spot Z5), and  $\text{AB}_2$  (spot Z6) phases are found as the new phases. All the patterns are blurry, which can be caused by multiple factors: besides the issues of imperfection in the sample polish and limited camera resolution, strains in the alloy can also influence the band contrasts.



**Figure 2.** SEM-BEI of the 8-h annealed sample. Structures of spots Z1 to Z6 and A to C were studied by EBSD. Compositions of spots Y1 to Y13 were measured by EDS.

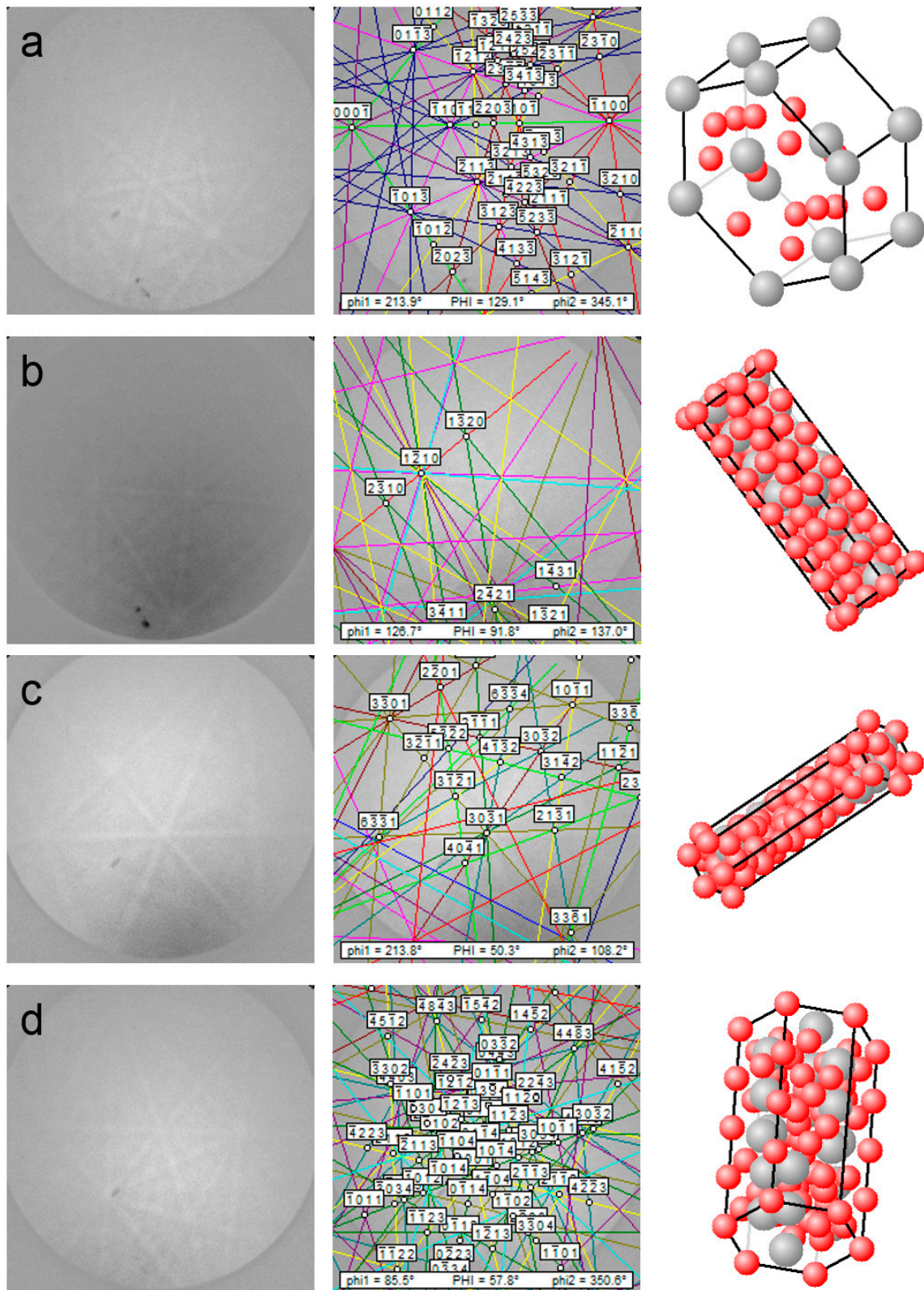
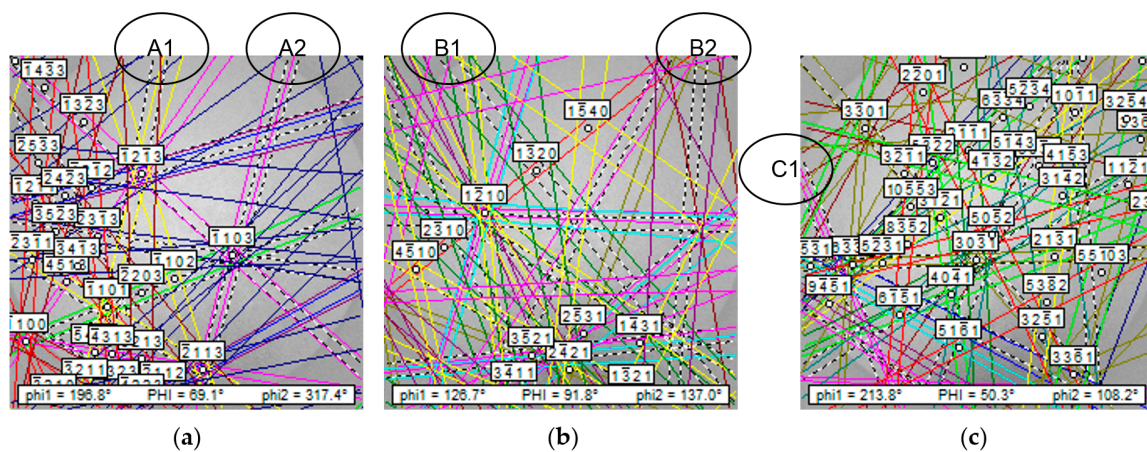
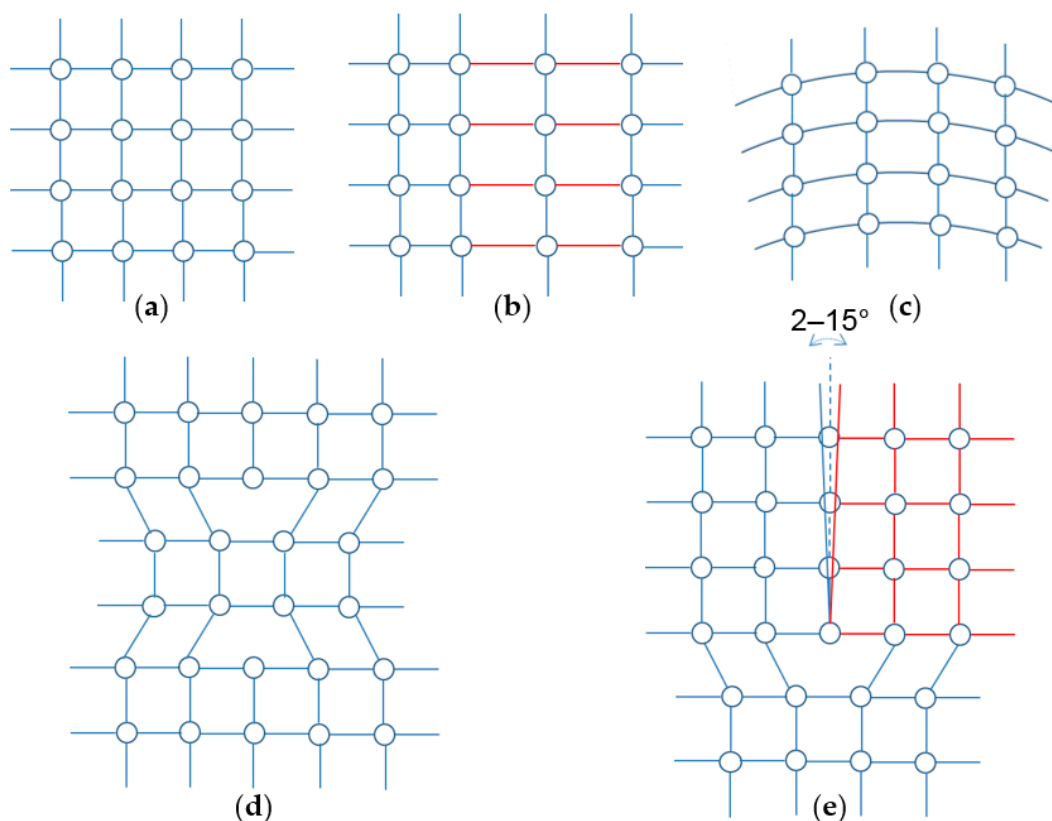


Figure 3. Cont.





**Figure 4.** Comparison of original and computer-generated EBSD patterns from spots (a) A:  $\text{LaNi}_5$ ; (b) B:  $\text{Ce}_2\text{Ni}_7$ ; and (c) C:  $\text{Pr}_2\text{Ni}_7$  of the 8-h annealed sample (Figure 2). Solid-color lines indicate the width of computer-generated band. Dashed-black lines show the width of actual band. A new band (B2) and bands with a slight rotation (A1), a shift (A2), a narrower width (B1), and a wider width (C1) are observed.



**Figure 5.** Schematic diagrams of (a) a regular crystal lattice; (b) a strained lattice with uniaxial lengthened bonds; (c) a bent lattice; (d) a distorted lattice with symmetric vacancy defects; and (e) a lattice with a subgrain boundary.

In this study, the La-Mg-Ni alloys were prepared by a solid-state method with Mg diffusing into the  $\text{LaNi}_5$  alloy. Therefore, both elastic and plastic strains were formed during the Mg-diffusion process and have strong influences on the EBSD pattern clarity. During the Mg-diffusion process, defects in the raw  $\text{LaNi}_5$  alloys were generated while new phases were formed. Physical and

chemical properties of the La-Mg-Ni alloys prepared by this method are affected by the distribution of defects, and compositions and abundances of constituent phases. Therefore, investigating the alloys' microstructures by the EBSD technique becomes important.

### 3.2. Phase Distribution

#### 3.2.1. Element Distribution

To fully characterize the alloys' microstructures, EDS elemental mappings were conducted on all four alloys (4 h-, 8 h-, 16 h-, and 32-h annealed samples), and the results are shown in Figure 6. While La and Ni distribute uniformly in all alloys, Mg shows a high concentration at the edges of all alloys. The EDS results of spots Y1 to Y13 in the SEM micrograph of the 8-h annealed sample (Figure 2) are listed in Table 1, which demonstrate the uneven distribution of Mg from the edge to center of alloy. Penetration of Mg into the 8-h annealed sample is about 100 microns. The value of Ni/(La + Mg) varies from 1.49 to 5.32, and the varying trend indicates that the phase changes along the longitudinal section (from one surface to another) of alloy. However, it must be stated that EDS is a semi-quantitative analysis method, so other technologies have to be combined with EDS to validate the phase distribution.

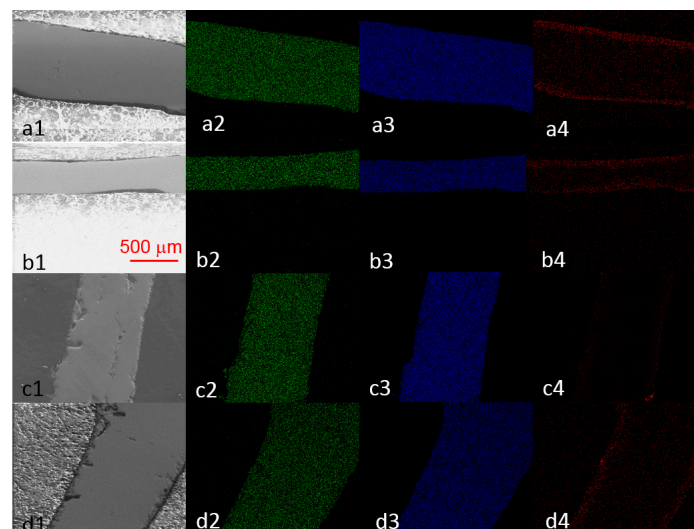


**Figure 6.** (a1,b1,c1,d1) SEM-BEIs and elemental mappings of (a2,b2,c2,d2) La, (a3,b3,c3,d3) Ni, and (a4,b4,c4,d4) Mg of the 4 h-, 8 h-, 16 h-, and 32-h annealed samples, respectively.

**Table 1.** Chemical compositions (in at%) from spots Y1 to Y13 of the 8-h annealed sample (Figure 2).

Spot	Mg	La	Ni	Ni/(La + Mg)
Y1	24.01	16.19	59.79	1.49
Y2	16.42	12.94	70.64	2.41
Y3	13.12	14.09	72.78	2.67
Y4	1.29	16.11	82.6	4.75
Y5	0.00	16.45	83.55	5.08
Y6	0.28	16.27	83.45	5.04
Y7	0.29	16.10	83.61	5.10
Y8	0.00	16.71	83.29	4.98
Y9	0.00	15.82	84.18	5.32
Y10	0.00	16.72	83.28	4.98
Y11	0.00	16.24	83.76	5.16
Y12	1.00	16.26	82.74	4.79
Y13	8.32	15.16	76.54	3.26

### 3.2.2. Phase Distribution

As an example, phase identification mapping by EBSD of the 16-h annealed sample is shown in Figure 7. Six phases, including  $\text{LaNi}_5$ ,  $\text{Ce}_2\text{Ni}_7$ ,  $\text{Pr}_2\text{Ni}_7$ ,  $\text{CeNi}_3$ ,  $\text{NbCr}_2$  (hexagonal), and Mg, can be identified. In the investigated area of the 16-h annealed sample, the  $\text{Pr}_5\text{Co}_{19}$ ,  $\text{Nd}_5\text{Co}_{19}$ , and  $\text{PuNi}_3$  structures are not found. A gradient of phase abundance can be observed for most phases.  $\text{LaNi}_5$ , the unreacted material, is concentrated in the center. While the diffuse-in Mg is concentrated at the edge,  $\text{Ce}_2\text{Ni}_7$ , one of the important target products [9], is also concentrated at the edge. Existence of pure Mg phase is validated in Supplement 2 with SEM micrographs (Figure S3) and EDS results showing high-Mg contents (Table S1).  $\text{Pr}_2\text{Ni}_7$ , another one of the target products, is located mainly between the  $\text{LaNi}_5$  and Mg phases. Abundances of the six phases in the investigated area are summarized in the table included in Figure 7. The  $\text{LaNi}_5$  abundance is 27.2%, and the combined abundance of  $\text{Ce}_2\text{Ni}_7$  and  $\text{Pr}_2\text{Ni}_7$  is 15.8%. The  $\text{CeNi}_3$  and  $\text{NbCr}_2$  phases are products from the overreaction of  $\text{Ce}_2\text{Ni}_7$  and  $\text{Pr}_2\text{Ni}_7$  with Mg. Future work will focus on increasing the  $\text{Ce}_2\text{Ni}_7$  and  $\text{Pr}_2\text{Ni}_7$  phase abundances.

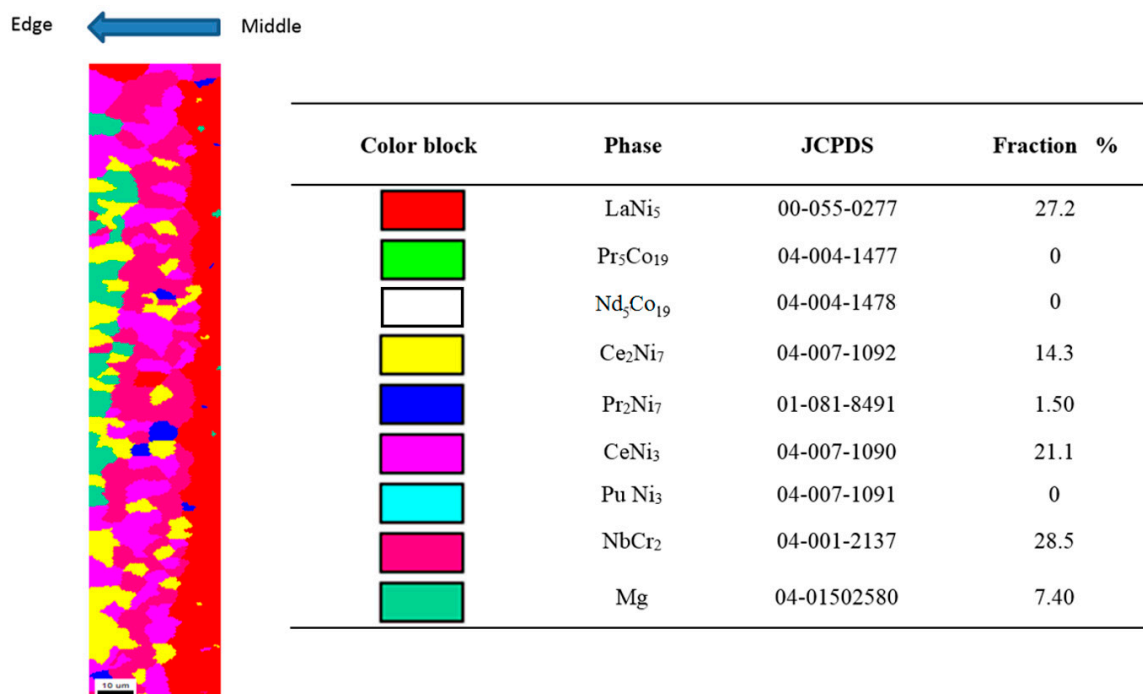


**Figure 7.** EBSD phase identification mapping and quantification of the 16-h annealed sample. The grain tolerance angle is  $15^\circ$ , and the minimum grain size is  $3 \mu\text{m}$ .

### 3.2.3. $\text{LaNi}_5$ and Mg Grain Distributions and Orientations

Inverse pole figure (IPF) and EBSD mapping, EBSD diffraction patterns, and crystal simulations of  $\text{LaNi}_5$  of the 16-h annealed sample are shown in Figure 8. In Figure 8a,b, color channels in red, green, and blue represent,  $[0001]$ ,  $[1010]$ , and  $[2110]$  of  $\text{LaNi}_5$ . Figure 8a shows only two grain orientations for  $\text{LaNi}_5$ . Grain orientations are described in the form of the Euler angle in Figure 8c,e. Figure 8a shows that grains with orientation 2 are isolated and much smaller in abundance than those with orientation 1. The right side of Figure 8a (the center of alloy) is a single  $\text{LaNi}_5$  grain without reacting with Mg. The interaction with Mg stopped at the grain boundary between the  $\text{LaNi}_5$  phase with orientation 1 and the  $\text{LaNi}_5$  phase with orientation 2. This is the proof that the inter-diffusion of Mg into the host  $\text{LaNi}_5$  alloy is through a specific direction (presumably along the  $ab$ -plane) and stops

at the grain boundary. Therefore, increasing the grain size of the host  $\text{LaNi}_5$  alloy can enhance the diffusion of Mg into the bulk.

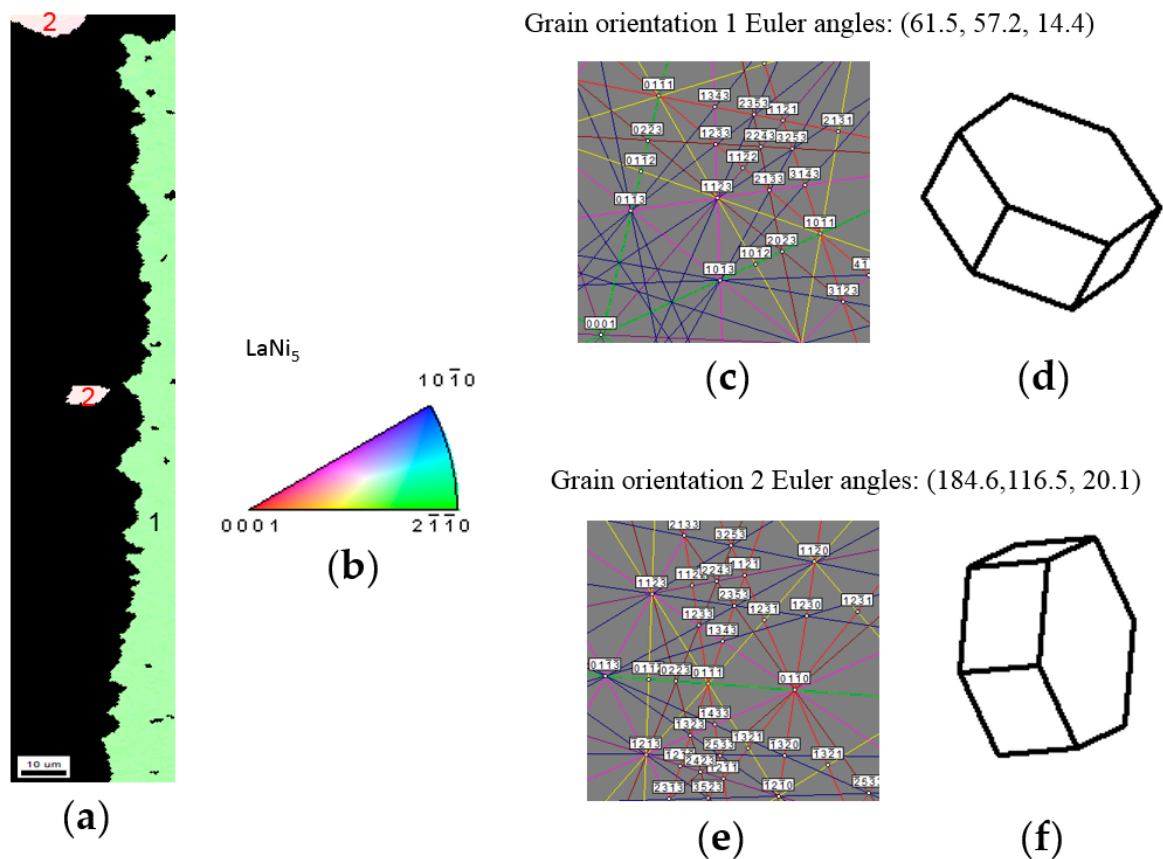


**Figure 8.** (a) IPF and EBSD mapping; (b) color assignment; (c) EBSD pattern for grain orientation 1 and (d) its corresponding crystal simulation; and (e) EBSD pattern for grain orientation 2 and (f) its corresponding crystal simulation of the  $\text{LaNi}_5$  phase of the 16-h annealed sample.

IPF and EBSD mapping, EBSD diffraction patterns, and crystal simulations of Mg of the 16-h annealed sample are shown in Figure 9. Three different crystallographic orientations are found for Mg. Grains with orientation 1 distribute at the edge of alloy and are the largest in size. Grains with orientation 3 distribute close to the center of alloy and are the smallest. After diffusing into the host, Mg first agglomerates into individual grains with the same crystallographic orientation (related to the host orientation) before reacting with the host to form the superlattice phases. It is interesting to find that the superlattice phases are formed by the reaction of  $\text{LaNi}_5$  with the Mg crystal but not the Mg vapor.

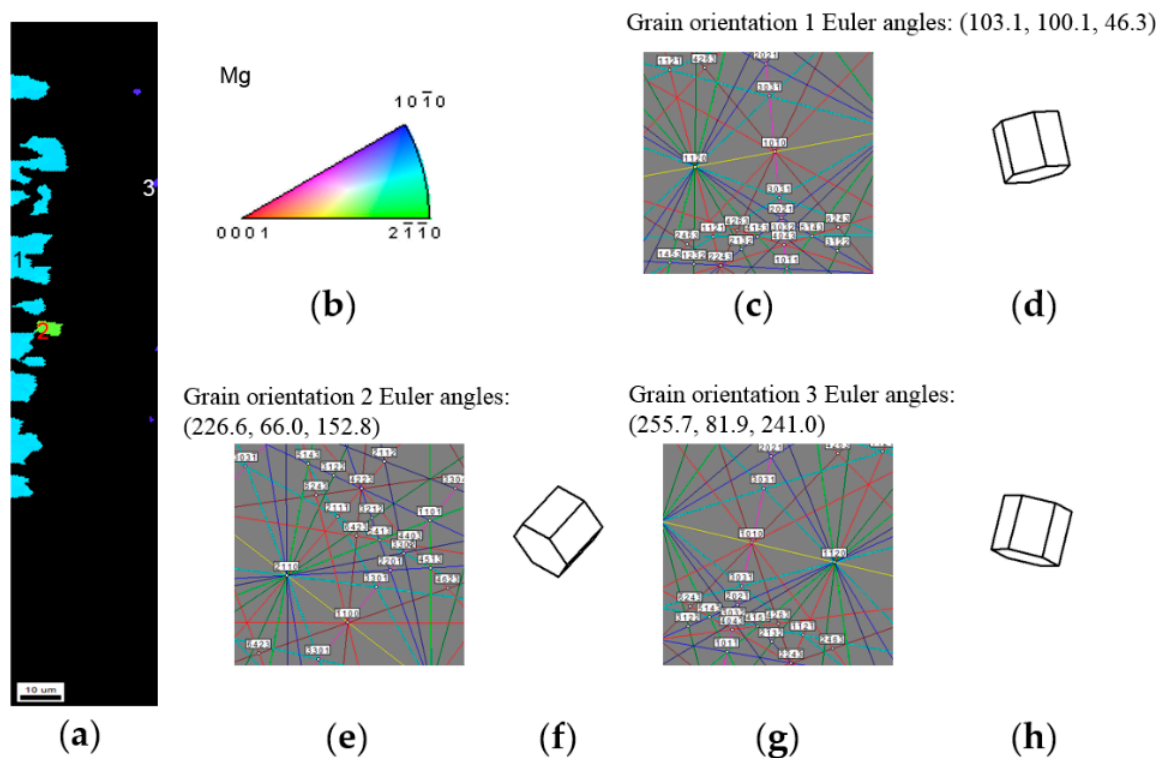


**Figure 9.** (a) IPF and EBSD mapping; (b) color assignment; (c) EBSD pattern for grain orientation 1 and (d) its corresponding crystal simulation; (e) EBSD pattern for grain orientation 2 and (f) its corresponding crystal simulation; and (g) EBSD pattern for grain orientation 3 and (h) its corresponding crystal simulation of the Mg phase of the 16-h annealed sample.

### 3.2.4. $\text{Ce}_2\text{Ni}_7$ and $\text{Pr}_2\text{Ni}_7$ Grain Distributions and Orientations

IPF and EBSD mapping, image quality (IQ) diffraction pattern and grain boundary map, and grain size distribution of  $\text{Ce}_2\text{Ni}_7$  of the 16-h annealed sample are shown in Figure 10. Unlike  $\text{LaNi}_5$  and Mg, the  $\text{Ce}_2\text{Ni}_7$  phase shows more grain orientations (Figure 10a). IQ patterns can be used to characterize the defect distribution in grains and is especially useful for the strain mapping [20]. Figure 10c shows that some grains are darker than the others, which indicates that concentrated defects and residual strains exist in these darker grains. A grain boundary is formed by the accumulation of edge dislocations. In this study, two types of boundaries are characterized: low-angle grain boundary (LAGB) and high-angle grain boundary (HAGB). LAGB subdivides a grain into two equiaxial cells and forms subgrains, which may increase the plastic deformation. In this study, we define the lattice misorientation of LAGB-separated grain zones to be from  $2^\circ$  to  $15^\circ$ . A grain boundary with a misorientation  $\geq 15^\circ$  is denoted as HAGB, which differentiates a grain from its initial microstructure and creates a new grain. Figure 10c indicates the grain boundary distribution of the  $\text{Ce}_2\text{Ni}_7$  phase in the 16-h annealed sample. Amount of LAGBs in the  $\text{Ce}_2\text{Ni}_7$  phase is 40.3%, which is much higher than that in the  $\text{LaNi}_5$  or Mg phase and suggests a high density of defects in the  $\text{Ce}_2\text{Ni}_7$  grains. Grain size distribution is shown in Figure 10d. Average grain diameter of the  $\text{Ce}_2\text{Ni}_7$  phase is  $7 \mu\text{m}$ . IPF and EBSD mapping, EBSD diffraction patterns, and crystal simulations of  $\text{Pr}_2\text{Ni}_7$  in the 16-h annealed sample are shown in Figure 11. Unlike  $\text{Ce}_2\text{Ni}_7$ , the  $\text{Pr}_2\text{Ni}_7$  phase has only two different orientations and a smaller grain size of about  $4 \mu\text{m}$ .

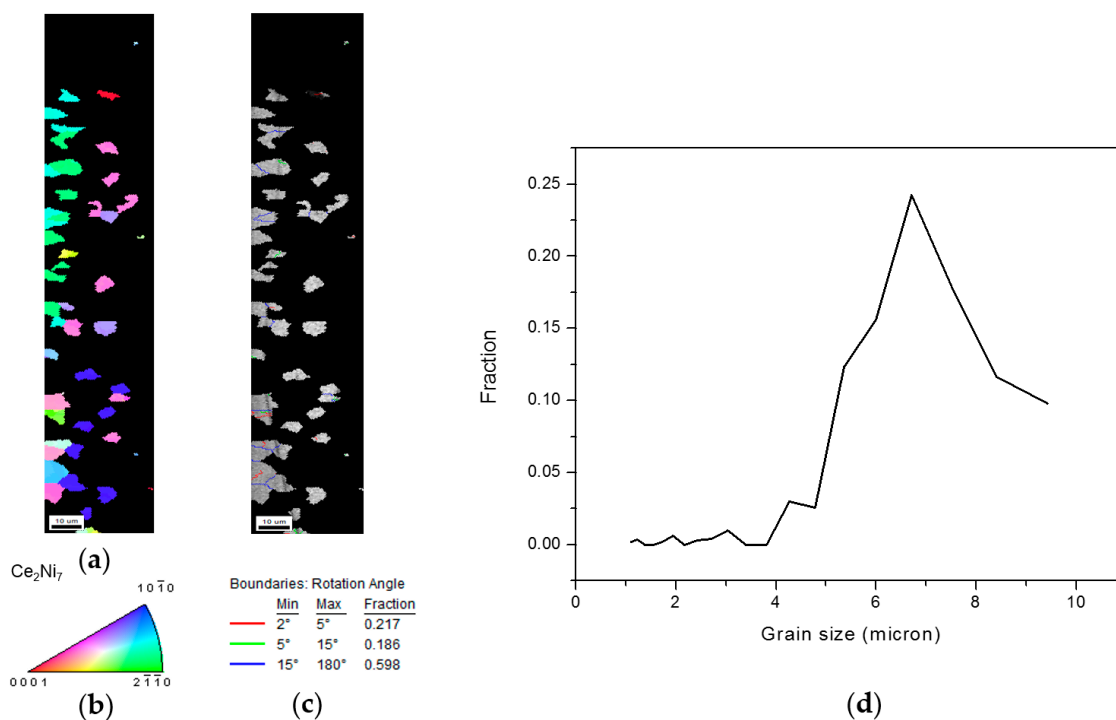


**Figure 10.** (a) IPF and EBSD mapping; (b) color assignment; (c) IQ diffraction pattern and grain boundary map; and (d) grain size distribution of the  $Ce_2Ni_7$  phase of the 16-h annealed sample.

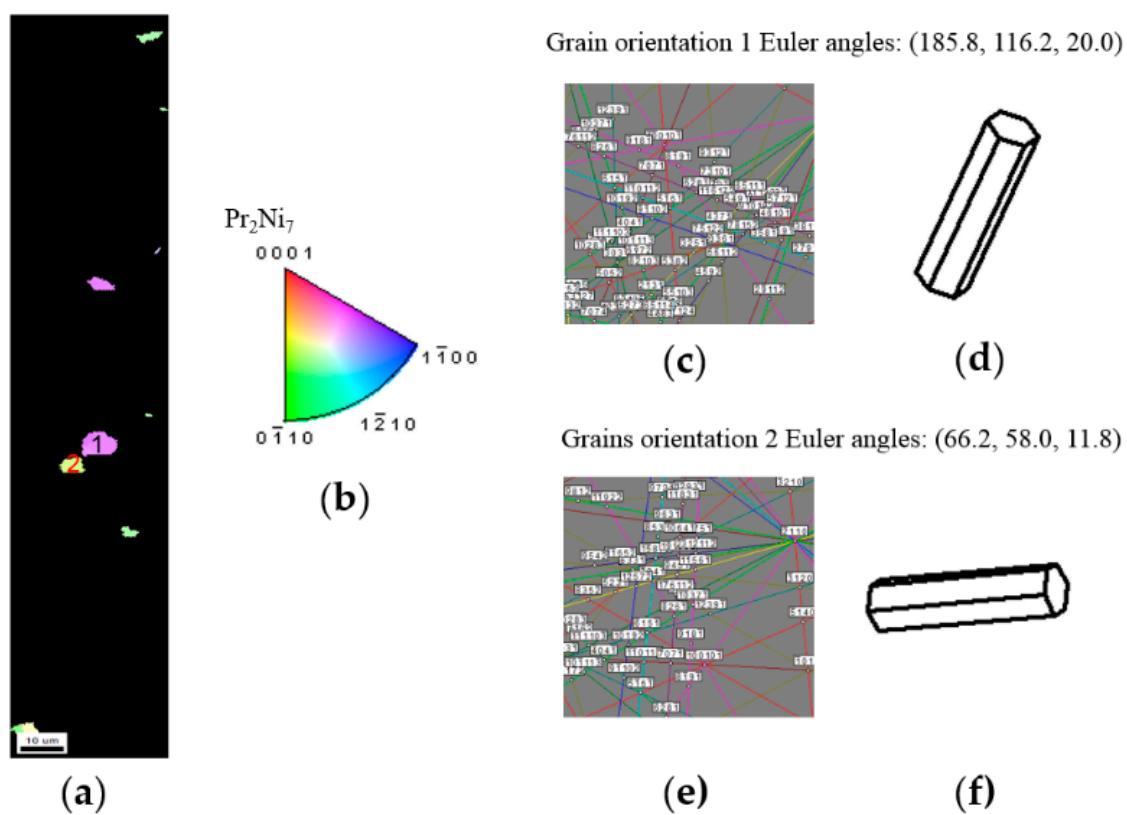


**Figure 11.** (a) IPF and EBSD mapping; (b) color assignment; (c) EBSD pattern for grain orientation 1 and (d) its corresponding crystal simulation; and (e) EBSD pattern for grain orientation 2 and (f) its corresponding crystal simulation of the  $Pr_2Ni_7$  phase of the 16-h annealed sample.

### 3.3. Alignment in Crystallographic Orientations

Figure 12a shows the EBSD phase identification mapping of the 8-h annealed sample. [0001]s of  $\text{LaNi}_5$  and  $\text{Pr}_2\text{Ni}_7$  in the green circle are found to be parallel to each other, and [0001]s of  $\text{LaNi}_5$  and  $\text{Ce}_2\text{Ni}_7$  in the black circle are also parallel (Figure 12b–e). This information gives a hint about the grain growth mechanism of the  $\text{A}_2\text{B}_7$ -type phases during the diffusion of Mg into the  $\text{AB}_5$  alloy. Structures of the La-Mg-Ni superlattice phases are composed of the  $\text{A}_2\text{B}_4$  and the  $\text{AB}_5$  slabs [23]. The alignments of  $\text{LaNi}_5$  and  $\text{Pr}_2\text{Ni}_7$  in the  $c$ -axis and  $\text{LaNi}_5$  and  $\text{Ce}_2\text{Ni}_7$  in the  $c$ -axis imply that Mg diffuses into  $\text{LaNi}_5$  and forms the  $\text{A}_2\text{B}_4$  slab through the  $ab$ -plane and, therefore, the  $c$ -axis orientation remains unchanged after the superlattice phase formation.

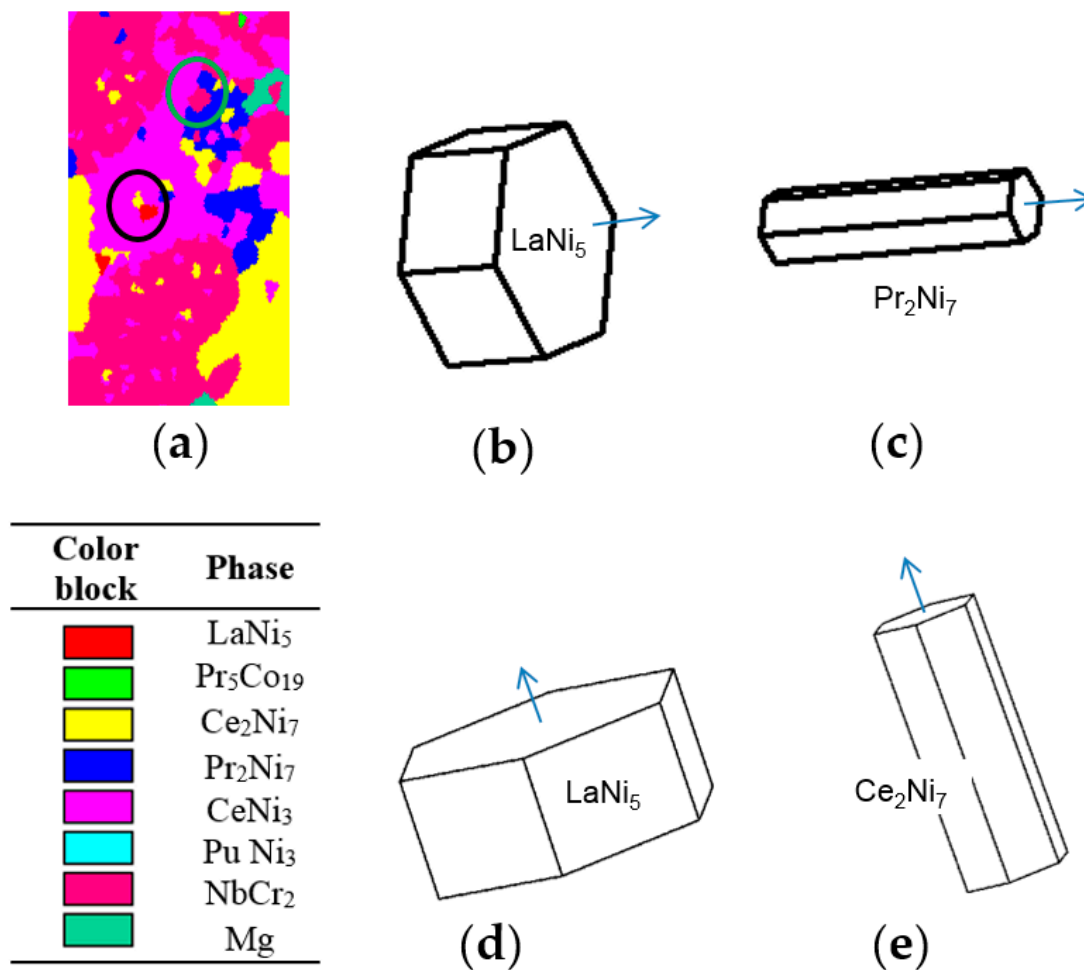


**Figure 12.** Crystallographic orientation alignments in [0001] demonstrated by (a) an IPF-EBSD map; orientations of (b)  $\text{LaNi}_5$  and (c) neighboring  $\text{Pr}_2\text{Ni}_7$  in the green circle; and orientations of (d)  $\text{LaNi}_5$  and (e) neighboring  $\text{Ce}_2\text{Ni}_7$  in the black circle of the 8-h annealed sample.

### 3.4. Effect of Process Temperature on Phase Development

EBSD mapping was performed in an area of  $30 \times 100$  square microns close to the edge of each sample. The results may not be very accurate because of the limited sampling areas and large variations in distribution of the superlattice phases. Nevertheless, the calculated phase abundances are compared in Table 2. The conversion from  $\text{LaNi}_5$  to other phases is more complete with the increase in process time and reaches 98.2 wt % at a processing time of 32 h. Abundance of the most desirable  $\text{Ce}_2\text{Ni}_7$  phase is about 25 wt % and not very sensitive to the processing time. Abundance of the  $\text{A}_2\text{B}_7$  phases (both  $\text{Ce}_2\text{Ni}_7$  and  $\text{Pr}_2\text{Ni}_7$ ) increases from 42.5 to 45.8 wt % and reduces to 39.2 wt % as

the processing time increases from 4 to 32 h. The unwanted AB<sub>2</sub> and AB<sub>3</sub> phases (with excessive Mg-content) cannot be eliminated with the increase in processing time. Future development work will focus on the reduction of the Mg-supply and/or addition of a second annealing treatment without Mg.

**Table 2.** Phase abundances (in wt %) obtained by EBSD mapping of the 4-h, 8-h, 16-h, and 32-h annealed samples with a grain tolerance angle of 5° and a minimum grain size of 2 µm.

Phase	4 h	8 h	16 h	32 h
LaNi <sub>5</sub>	13.2	5.5	4.2	1.8
Ce <sub>2</sub> Ni <sub>7</sub>	23.5	27.3	27.6	25.5
Pr <sub>2</sub> Ni <sub>7</sub>	19.0	18.5	16.3	13.7
CeNi <sub>3</sub>	22.6	19.5	26.4	21.0
PuNi <sub>3</sub>	0.5	0.2	0.5	0.5
NbCr <sub>2</sub>	16.2	25.5	22.3	30.3
Mg	4.9	3.4	2.8	7.2

Grain size distributions of all four samples are also compared and listed in Table 3. The 4-h annealed sample has a heavy proportion of medium-size grains (5–12 µm) while the 8-h annealed sample has a much higher percentage of small grains (1–5 µm). Longer processing time (16- and 32-h) recovers the percentage of medium-size grains. The reason for the grain size evolution is not clear and requires further studies. The last comparison is on the distribution of misorientation angle in the grain boundary, which is shown in Table 4. Amount of HAGBs (15 to 180°) decreases with the increase in process time, which suggests the occurrence of lattice cracking.

**Table 3.** Grain size distributions of the 4-h, 8-h, 16-h, and 32-h annealed samples.

Grain Size (µm)	4 h	8 h	16 h	32 h
1 to 5	24%	79%	35%	37%
5 to 12	61%	16%	48%	49%
>12	15%	5%	16%	14%

**Table 4.** Grain boundary distributions of the 4-h, 8-h, 16-h, and 32-h annealed samples.

Grain Boundary (°)	4 h	8 h	16 h	32 h
2 to 5	11.3%	14.4%	22.3%	22.1%
5 to 15	4.3%	2.5%	0.7%	11.4%
15 to 180	84.4%	83.1%	77.0%	55.5%

#### 4. Conclusions

A gaseous-state Mg-diffusion into an AB<sub>5</sub> metal hydride alloy is demonstrated as an effective method to convert a LaNi<sub>5</sub> alloy to a multi-phase superlattice alloy. Four La-Mg-Ni superlattice phases are identified by EBSD in the products: Ce<sub>2</sub>Ni<sub>7</sub>, Pr<sub>2</sub>Ni<sub>7</sub>, CeNi<sub>3</sub>, and PuNi<sub>3</sub>. Additionally, Mg and AB<sub>2</sub> (with the hexagonal NbCr<sub>2</sub> structure) phases are also found. Longer process time increases the LaNi<sub>5</sub> conversion rate but shows no significant effect on increasing the abundance of the most desirable Ce<sub>2</sub>Ni<sub>7</sub> phase. Defects are found abundantly in the Ce<sub>2</sub>Ni<sub>7</sub> and Pr<sub>2</sub>Ni<sub>7</sub> phases by EBSD, and distributions of the superlattice phases are not uniform. Future activities in reducing the Mg-loading, addition of a second annealing treatment, and increasing the initial grain size of the host alloy are suggested based on the findings in this study.

**Supplementary Materials:** The following are available online at <http://www.mdpi.com/2313-0105/3/4/40/s1>.

**Acknowledgments:** The authors would like to thank the following individuals for their help: Alan Chan, Jean Nei, and Diana Wong from BASF—Ovonic.

**Author Contributions:** Xin Zhao prepared the sample and Shuli Yan performed the EBSD study. Kwo-Hsiung and Simon Ng provided guidance and helped in manuscript preparation.

**Conflicts of Interest:** The authors declare no conflict of interest.

## Abbreviations

RE	Rare earth
MH	Metal hydride
Ni/MH	Nickel/metal hydride
HRD	High-rate dischargeability
EBSD	Electron backscatter diffraction
SEM	Scanning electron microscope
EDS	Energy dispersive spectroscopy
BEI	Backscattered electron image
SSD	Statistically stored dislocations
GND	Geometrically necessary dislocations
IPF	Inverse pole figure
IQ	Image quality
LAGB	Low-angle grain boundary
HAGB	High-angle grain boundary

## References

1. Yasuoka, S.; Magari, Y.; Murata, T.; Tanaka, T.; Ishida, J.; Nakamura, H.; Nohma, T.; Kihara, M.; Baba, Y.; Teraoka, H. Development of high-capacity nickel-metal hydride batteries using superlattice hydrogen-absorbing alloys. *J. Power Sources* **2006**, *156*, 662–666. [[CrossRef](#)]
2. Teraoka, H. Development of Low Self-Discharge Nickel-Metal Hydride Battery. Available online: <http://www.scribd.com/doc/9704685/Teraoka-Article-En> (accessed on 9 April 2016).
3. Kai, T.; Ishida, J.; Yasuoka, S.; Takeno, K. The effect of nickel-metal hydride battery's characteristics with structure of the alloy. In Proceedings of the 54th Battery Symposium in Japan, Osaka, Japan, 7–9 October 2013; p. 210.
4. Takasaki, T.; Nishimura, K.; Saito, M.; Fukunaga, H.; Iwaki, T.; Sakai, T. Cobalt-free nickel-metal hydride battery for industrial applications. *J. Alloys Compd.* **2013**, *580*, S378–S381. [[CrossRef](#)]
5. Teraoka, H. Development of Ni-MH EThSS with Lifetime and Performance Estimation Technology. In Proceedings of the 34th International Battery Seminar & Exhibit, Fort Lauderdale, FL, USA, 20–23 March 2017.
6. Teraoka, H. Ni-MH Stationary Energy Storage: Extreme Temperature & Long Life Developments. In Proceedings of the 33th International Battery Seminar & Exhibit, Fort Lauderdale, FL, USA, 21–24 March 2016.
7. Teraoka, H. Development of Highly Durable and Long Life Ni-MH Batteries for Energy Storage Systems. In Proceedings of the 32th International Battery Seminar & Exhibit, Fort Lauderdale, FL, USA, 9–12 March 2015.
8. Ouchi, T.; Young, K.; Moghe, D. Reviews on the Japanese Patent Applications regarding nickel/metal hydride batteries. *Batteries* **2016**, *2*, 21. [[CrossRef](#)]
9. Young, K.; Ouchi, T.; Nei, J.; Koch, J.M.; Lien, Y. Comparison among constituent phases in superlattice metal hydride alloys for battery applications. *Batteries* **2017**, *3*, 34. [[CrossRef](#)]
10. Young, K.; Yasuoka, S. Past, present, and future of metal hydride alloys in nickel-metal hydride batteries. In Proceedings of the 14th International Symposium on Metal-Hydrogen Systems, Manchester, UK, 21–25 July 2014.

11. Hayakawa, H.; Enoki, H.; Akiba, E. Annealing conditions with Mg vapor-pressure control and hydrogen storage characteristic of  $\text{La}_4\text{MgNi}_{19}$  hydrogen storage alloy. *Jpn. Inst. Met.* **2006**, *70*, 158–161. (In Japanese) [[CrossRef](#)]
12. Crivello, J.-C.; Zhang, J.; Latroche, M. Structural stability of  $\text{AB}_y$  phases in the (La,Mg)–Ni system obtained by density functional theory calculations. *J. Phys. Chem.* **2011**, *115*, 25470–25478.
13. Crivello, J.-C.; Gupta, M.; Latroche, M. First principles calculations of  $(\text{La,Mg})_2\text{Ni}_7$  hydrides. *J. Alloys Compd.* **2015**, *645*, S5–S8. [[CrossRef](#)]
14. Young, K.; Ouchi, T.; Huang, B. Effects of annealing and stoichiometry to (Nd, Mg)(Ni, Al) $_{3.5}$  metal hydride alloys. *J. Power Sources* **2012**, *215*, 152–159. [[CrossRef](#)]
15. Zhao, X.; Li, B.; Zhu, X.; Han, S.; Yan, H.; Ji, L.; Wang, L.; Li, J.; Xiong, W.; Jia, T. Preparation Method of Low-Melting Point Metal Alloy. Chinese Patent Application 201,511,015,059, 31 December 2015.
16. Young, K.; Chang, S.; Lin, X. C14 Laves phase metal hydride alloys for Ni/MH batteries applications. *Batteries* **2017**, *3*, 27. [[CrossRef](#)]
17. Matiland, T.; Sitzman, S. Electron backscatter diffraction (EBSD) technique and materials characterizations examples. In *Scanning Microscopy for Nanotechnology Techniques and Applications*; Zhou, W., Wang, Z.L., Eds.; Springer: New York, NY, USA, 2007.
18. Young, K.; Ouchi, T.; Liu, Y.; Reichman, B.; Mays, W.; Fetcenko, M.A. Structural and electrochemical properties of  $\text{Ti}_x\text{Zr}_{7-x}\text{Ni}_{10}$ . *J. Alloy. Compd.* **2009**, *480*, 521–528. [[CrossRef](#)]
19. Liu, Y.; Young, K. Microstructure investigation on metal hydride alloys by electron backscatter diffraction technique. *Batteries* **2016**, *2*, 26. [[CrossRef](#)]
20. Shen, H.; Young, K.; Meng, T.; Bendersky, L.A. Clean grain boundary found in C14/body-center-cubic multi-phase metal hydride alloys. *Batteries* **2016**, *2*, 22. [[CrossRef](#)]
21. Liu, J.; Han, S.; Li, Y.; Zhang, L.; Zhao, Y.; Yang, S. Phase structures and electrochemical properties of La–Mg–Ni-based hydrogen storage alloys with superlattice structure. *Int. J. Hydrogen Energy* **2016**, *41*, 20261–20275. [[CrossRef](#)]
22. Buschow, K.H.; Van Mal, H.H. Phase relations and hydrogen absorption in the lanthanum-nickel system. *J. Less Common Met.* **1972**, *29*, 203–210. [[CrossRef](#)]
23. Young, K.; Nei, J. The current status of hydrogen storage alloy development for electrochemical applications. *Materials* **2013**, *6*, 4574–4608. [[CrossRef](#)] [[PubMed](#)]
24. Chang, S.; Young, K.-H.; Nei, J.; Fierro, C. Reviews on the US Patents regarding nickel/metal hydride batteries. *Batteries* **2016**, *2*, 10. [[CrossRef](#)]
25. Young, K.; Ouchi, T.; Nei, J.; Yasuoka, S. Fe-substitution for Ni in misch metal-based superlattice hydrogen absorbing alloys—Part 1. Structural, hydrogen storage, and electrochemical properties. *Batteries* **2016**, *2*, 34. [[CrossRef](#)]
26. Wright, S.I.; Nowell, M.M.; Field, D.P. A review of strain analysis using electron backscatter diffraction. *Microsc. Microanal.* **2011**, *17*, 316–329. [[CrossRef](#)] [[PubMed](#)]
27. Winkelmann, A. Dynamical effects of anisotropic inelastic scattering in electron backscatter diffraction. *Ultramicroscopy* **2008**, *108*, 1546–1550. [[CrossRef](#)] [[PubMed](#)]
28. Keller, R.R.; Roshko, A.; Geiss, R.H.; Bertness, K.A.; Quinn, T.P. EBSD measurement of strains in GaAs due to oxidation of buried AlGaAs layers. *Microelectron. Eng.* **2004**, *75*, 96–102. [[CrossRef](#)]

